Supplementary information

Control and single-shot readout of an ion embedded in a nanophotonic cavity

Jonathan M. Kindem, Andrei Ruskuc, John G. Bartholomew, Jake Rochman, Yan Qi Huan & Andrei Faraon✉

Supplementary information: Control and single-shot readout of an ion embedded in a nanophotonic cavity

Jonathan M. Kindem[1,2], Andrei Ruskuc[1,2], John G. Bartholomew[1,2], Jake Rochman[1,2], Yan Qi Huan[1,2], and Andrei Faraon[1,2,*]

[1]Kavli Nanoscience Institute and Thomas J. Watson, Sr., Laboratory of Applied Physics, California Institute of Technology, Pasadena, California 91125, USA
[2]Institute for Quantum Information and Matter, California Institute of Technology, Pasadena, California 91125, USA
[*]faraon@caltech.edu

Dated: January 13, 2020

Supplementary Information

List of Figures

1   Detailed experimental setup

Fig. S1A shows a schematic of the optical network used in these experiments. The ions in the cavity are optically addressed using two continuous-wave lasers. The state of the ions is read out on transition A (Fig. 1A) using a Ti:Sapphire laser (M2 Solstis) and optical pumping on transition F is performed using an external-cavity diode laser (ECDL, Toptica DLPro).

A small portion of the Ti:Sapph is picked off to enable locking to a high-finesse Fabry-Perot cavity (Stable Laser Systems) that serves as a stable long-term frequency reference. A fibre-based phase-modulator (EOSpace) imposes variable-frequency sidebands onto the light before the reference cavity and the first-order sideband is locked to the cavity using the standard Pound-Drever-Hall (PDH) technique. Scanning the frequency of this sideband enables quasi-continuous scans over a 3 GHz range while locked to a single longitudinal mode of the reference cavity. The wavelength of the laser is monitored using a wavemeter (Bristol Instruments) to reliably lock to the same longitudinal mode of the cavity. The ECDL is held at a fixed frequency with respect to the Ti:Sapph by measuring the beat note between the two lasers on a fast photodiode (Newport) and feeding back to the ECDL current and piezo control.
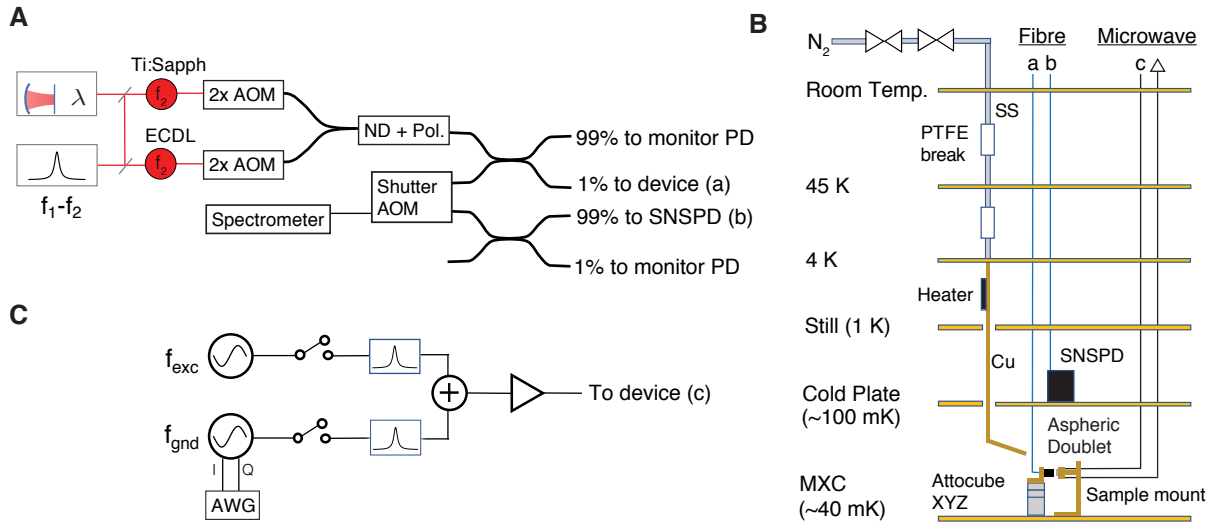

Figure S1: Additional details of experimental setup. A) Optical network for optical manipulation and readout of single ions. Light from two single-mode lasers (Ti:Sapph and ECDL) are modulated by AOMs, coupled into fibre, and passed through neutral density (ND) filters and a polarisation controller. Light is sent to the device in the dilution refrigerator using a 99/1 fibre splitter, with 1% going to the device (a) and 99% monitored on a photodiode. Light reflected from the device is directed to an acousto-optic modulator (AOM) before being detected using a WSi_2 superconducting nanowire single photon detector (SNSPD) (b). The reflected signal can also be routed to a spectrometer for alignment and tuning of the device. A small portion of the Ti:Sapph is used to establish an offset-frequency lock to a Fabry-Perot reference cavity and is monitored by a wavemeter. The ECDL is held at a fixed frequency with respect to the Ti:Sapph by measuring the beat note between the two lasers on a fast photodiode. B) Schematic of experiment inside the dilution refrigerator. Light from the optical network in (A) is coupled into the device via an aspheric doublet mounted on an Attocube XYZ stack. Tuning is accomplished by depositing N_2 on the device as described in the text. C) Microwave setup for manipulating spin transitions. Two microwave frequency sources are sent through switches and narrow-band filters before being combined, amplified, and sent to the device in the dilution refrigerator (c).

Each laser is independently amplitude-modulated using two free-space acousto-optic modulators (AOMs) in double-pass configuration with total extinction of ~ 120 dBm. The lasers are coupled into fibre and combined using a fibre-based beamsplitter. A set of variable attenuators and polarisation controllers allow for further adjustment of the amplitude and polarisation of the light that passes through a 99/1 fibre splitter before being directed to the device. Light reflected or emitted from the device is directed by the 99/1 splitter through an additional free-space AOM shutter before being detected by a WSi_2 superconducting nanowire single photon detector (SNSPD) (*S1*). This detector has high efficiency ($\sim 75\%$) and low intrinsic dark counts (< 1 Hz). The AOM shutter serves to protect the SNSPD from latching during preparation and readout pulses. All fibre connections are spliced when possible to minimise reflections and additional losses. The total system detection efficiency (probability of detecting a photon emitted by an ion in the cavity) is $\sim 1\%$.

The current system detection efficiency is primarily limited by the undercoupling of the cavity ($\kappa_{in}/\kappa \sim 0.14$) and fibre-to-waveguide coupling ($\sim 24\%$). Previous work from our group has demonstrated that it is realistic to achieve critical coupling ($\kappa_{in}/\kappa \sim 0.5$) in FIB-milled cavities in YVO (*S2*). Further improvements could be achieved by using SNSPDs optimized for 984 nm and using a shutter with lower insertion loss (currently 3 dB). With these improvements, it is reasonable to expect a factor of 10 increase in detection efficiency (i.e. total detection efficiencies of up to $\sim 10\%$) with the current design. Additional modifications to the nanocavity design and fabrication would allow for direct fibre coupling to these devices similar to that shown in Ref. (*S3*), which would enable significantly larger improvements to the overall detection efficiency. An alternative approach to device fabrication could use hybrid resonators based on GaAs on YVO as has been shown with silicon on YSO (*S4*, *S5*). In addition to the possibility of increased Q/V and scalability, this approach is also amenable to high fibre-waveguide coupling efficiencies (*S6*, *S7*).

A broadband supercontinuum source (Fianium WhiteLase Micro) and a spectrometer (Princeton Instruments SP-2750, PIXIS 2KB eXcelon) are used for measuring the cavity reflection spectrum when aligning and tuning the device.

Fig. S1B shows a schematic of the experimental setup inside of a Bluefors LD250 dilution refrigerator. The device is held stationary on a copper sample mount on the mixing chamber (MXC) plate. Light is coupled into and out of the device from fibre using an aspheric doublet mounted on an XYZ piezo-stage (Attocube) that allows for optimization of this coupling at dilution fridge temperatures.

Devices are tuned onto resonance with the ion transition of interest by nitrogen deposition (*S8*). To implement this in the dilution refrigerator, a gas tuning line is installed from room temperature down to the mixing chamber (Fig. S1B). This tuning line consists of stainless-steel (SS) tubing from room temperature to 4 K with the tubing thermalised at each stage and isolated between stages by a PTFE break. From 4 K to the mixing chamber plate, the tuning line consists of a free-hanging copper tube that is thermally isolated from the components below 4 K. The output of this line is directed onto the sample on the mixing chamber plate. A resistive heater attached to the tuning line near the 4 K stage enables warming of the line such that gas flows through the line without freezing and is deposited onto the device. Careful adjustment of the heater power allows for fine red-tuning of the cavity resonance at rates < 0.1 nm/minute. The cavities can be detuned by sublimation of the frozen nitrogen through optical heating of the device using $\sim 100\ \mu$W of laser power resonant with the cavity mode.

Fig. S1C shows the setup for microwave control of single ions. Microwave tones to drive the ground and excited state transitions are generated using two signal generators (Stanford Research Systems SG380). The amplitude and phase of the pulses used on the ground state transition are controlled using IQ modulation driven by a fast function generator (Tektronix AWG5204). Microwave tones pass through a set of microwave switches (Minicircuits ZASWA-2-50DR+) and narrow-band filters to provide additional extinction before being combined, amplified, and sent to the device in the dilution fridge. To ensure adequate microwave power at the device for these initial measurements, minimal attenuation is used on the input coaxial lines inside the fridge with a single 20 dB attenuator on the still plate and 0 dB attenuators on the other plates.

A gold coplanar waveguide is fabricated next to the optical cavity to allow for microwave manipulation of the $|0\rangle_g \rightarrow |1\rangle_g$ and $|0\rangle_e \rightarrow |1\rangle_e$ transitions. The centre strip of this waveguide is 60 μm wide with a spacing of 30 μm to the ground plane. The optical device sits inside this 30 μm gap. The YVO chip sits inside a microwave launch board (Rogers AD1000, fabricated by Hughes Circuits) with SMP connectors on both input and output. This launch board is wire-bonded to the chip with as many wirebonds as possible to give additional cooling through the surface.

2 Identifying single ^{171}Yb ions

2.1 Energy structure of ^{171}Yb:YVO

The $4f^{13}$ configuration of Yb^{3+} consists of two electronic multiplets, $^2F_{7/2}$ (ground state) and $^2F_{5/2}$ (excited state), that are split by the crystal field of YVO into four and three Kramers doublets, respectively. The optical transition of interest is between the lowest energy doublets of the ground state and excited state ($^2F_{7/2}(0) \rightarrow {}^2F_{5/2}(0)$), which occurs at approximately 984.5 nm for Yb^{3+} doped into YVO. At cryogenic temperatures, the Kramers doublets can be treated as spin-1/2 systems and described using an effective spin Hamiltonian (*S9*). For isotopes with non-zero nuclear spin, the hyperfine interaction adds additional energy structure. The ^{171}Yb isotope is unique among the rare-earth ions as the only stable Kramers ion with nuclear spin $I = 1/2$, which gives rise to the simplest possible level structure with both electron and nuclear spin. Additional discussion on the level-structure and effective spin Hamiltonian can be found in (*S10*).

The energy level structure of the lowest crystal field levels of ^{171}Yb:YVO at zero-field is shown in Fig. S2. The red (blue) lines correspond to optical transitions allowed for light polarised parallel (perpendicular) to the c-axis of the crystal. The red transitions are the Purcell-enhanced transitions co-polarised with the cavity mode. The transitions $|0\rangle_g \rightarrow |0\rangle_e$ and $|1\rangle_e \rightarrow |1\rangle_g$ are forbidden at zero-field by symmetry.
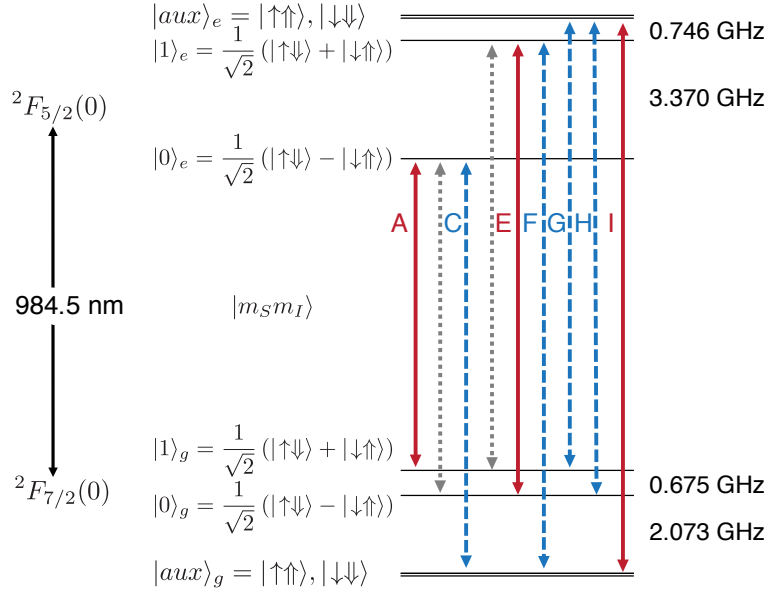

Figure S2: Detailed level structure of ^{171}Yb:YVO at zero-field (*S10*). We denote the electron spin component of the state as $|\uparrow\rangle \equiv \left|S_z = \frac{1}{2}\right\rangle$, $|\downarrow\rangle \equiv \left|S_z = -\frac{1}{2}\right\rangle$ and the nuclear spin component as $|\Uparrow\rangle \equiv \left|I_z = \frac{1}{2}\right\rangle$, $|\Downarrow\rangle \equiv \left|I_z = -\frac{1}{2}\right\rangle$. States $|0\rangle_g$ and $|1\rangle_g$ form the spin qubit used in this work. States $|\uparrow\Uparrow\rangle$ and $|\downarrow\Downarrow\rangle$ are degenerate in the absence of strain and are referred to throughout the text as $|aux\rangle$. Optical transitions allowed for $E \parallel c$ are shown in red (solid), while transitions allowed for $E \perp c$ are shown in blue (dashed).

2.2 PLE scans

To determine whether an isolated peak observed in the photoluminescence excitation (PLE) scans shown in Fig. 2A corresponds to a ^{171}Yb ion, we investigate the energy level structure using optical pumping. The readout laser is tuned on resonance with one of these peaks and a second laser is scanned across transition F. If an observed peak corresponds to the A transition of a ^{171}Yb ion, the pump laser will move population into the qubit subspace as it comes into resonance with F and result in an increase in counts after the readout pulse. Fig. S3 shows examples of these scans performed on the ions labeled as X and Y in Fig. 2A. A small splitting of transition F is observed that is unexpected for an ion in a D_{2d} symmetric site at zero magnetic field. Further investigations into the behaviour of this splitting with

applied magnetic field confirm that this is not due to a residual magnetic field at the ion.

This splitting is attributed to the ions occupying strained or otherwise distorted sites in the crystal. Here, we isolate single ions by working in the tails of the inhomogeneous distribution arising from variations in the local environment within the crystal. As a result, we are, in practice, preferentially selecting for strained ions. A distortion of the local crystal lattice can reduce the site symmetry of the ion, which would lead to a breaking of the degeneracy of the lowest energy levels in the ground state (i.e. break the degeneracy of $|aux\rangle_g$) (S11). Further studies are necessary to understand the nature and cause of this strain and its consequences for the properties of the ion. Depending on the resulting site symmetry of the ion, these ions could potentially now possess a first-order DC Stark shift (S12). This would have negative implications for long-term optical spectral diffusion due to fluctuating electric fields, but would also open the door to tuning and stabilization of the optical transition through applied DC electric fields.
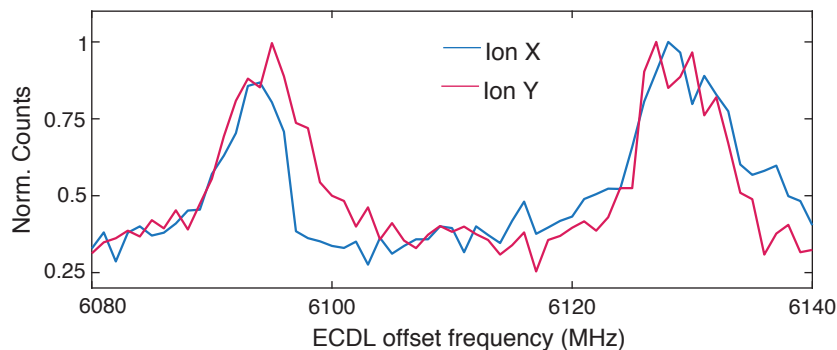

Figure S3: Offset frequency scans to verify potential ^{171}Yb ions identified in Fig. 2A. A readout pulse is tuned on resonance with an isolated peak and a second laser is used to perform optical pumping around transition F.
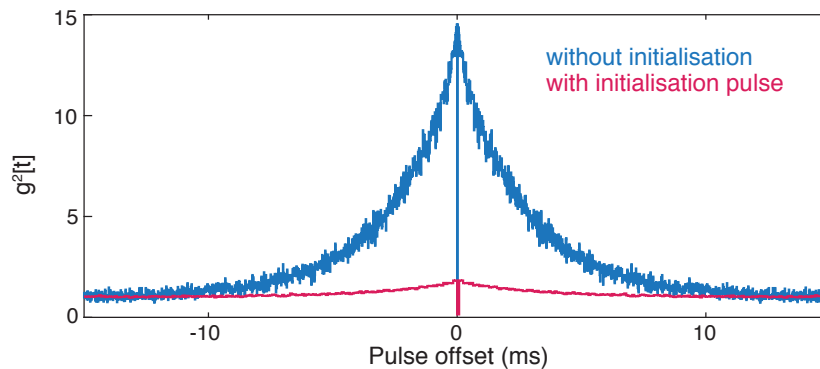

Figure S4: Measurement of pulsed second-order autocorrelation on ion X with a single initialisation pulse on transition C (red) and no initialisation pulse (blue).

2.3 Bunching behaviour in $g^{(2)}[t]$

The bunching behaviour observed in the measurement of $g^{(2)}[t]$ for $t > 0$ (Fig. 2B) is expected for a multi-level system with long-lived shelving states, where the amplitude of the bunching corresponds to the ratio of effective decay rates into and out of $|1\rangle_g$ (S13). The single initialisation pulse is not sufficient in this case to completely initialise the ion into $|1\rangle_g$ before each readout, but was chosen to enable faster repetition of the experiment. We expect that this effect would not be observed with full initialisation of the ion before each readout. This bunching could also be attributed to spectral diffusion or blinking (S14). Additional $g^{(2)}[t]$ measurements performed on ions identified as zero-spin isotopes at zero-field (i.e. no shelving levels) do not exhibit this bunching, providing further evidence that this is due to the multiple long-lived levels of ^{171}Yb at zero-field.

To show that the observed bunching behaviour is related to a population effect, this measurement was repeated without any initialisation into state $|1\rangle_g$ as shown in Fig. S4. In this case, the rate of pumping into $|1\rangle_g$ is reduced, while the effective pumping rate out of $|1\rangle_g$ is held constant. This leads to a drastically increased bunching behaviour for $t > 0$ as shown.

Second-order intensity correlation measurements performed on ion Y show similar behaviour and give $g^{(2)}[0] = 0.30 \pm 0.03$. These results indicate that we have correctly identified X and Y as single $^{171}\text{Yb}^{3+}$ ions.

3   Purcell enhancement and optical branching ratio

3.1   Predicted Purcell enhancement

The polarised oscillator strength of the $^2F_{7/2}(0) \rightarrow {}^2F_{5/2}(0)$ transition for light polarised along c (i.e. transitions A, E, I) was determined to be $f = 1.4 \times 10^{-5}$ from bulk absorption measurements (*S10*). Note that here we are using the real-cavity local field correction factor between absorption and oscillator strength (*S15*, *S16*). The transition dipole moment, μ, is related to the polarised oscillator strength (*S17*) as

$$|\mu|^2 = \frac{\hbar e^2 f}{2 m_e \omega},$$ (S1)

where m_e is the mass of the electron, e is the charge of the electron, and ω is the frequency of the optical transition. The dipole moment of these transitions (A, E, and I) is then $|\mu| = 1.06 \times 10^{-31}$ C $\cdot$ m, which corresponds to an emission rate for $E \parallel c$ of $\gamma_\parallel = 1/(763\,\mu\text{s})$. Using the bulk excited state lifetime of $267\,\mu\text{s}$, this gives a branching ratio for decay with $E \parallel c$ of $\beta_\parallel \sim 0.35$.

The optical decay rate of the atom in the nanophotonic cavity, γ_{cav}, is enhanced from its free space value $\gamma_0 = 1/(267\,\mu\text{s})$ by

$$\frac{\gamma_{cav}}{\gamma_0} = 1 + \frac{4g^2}{\kappa\gamma_0} = 1 + \eta,$$ (S2)

where we have assumed that the cavity is resonant with the optical transition. Here, η is referred to as the effective Purcell factor to distinguish from the enhancement of the cavity-coupled transition by F_p and the resulting overall change in the lifetime determined by the branching ratio (i.e. $\eta = \beta_\parallel F_p$). The coupling between atom and cavity field is described by the single photon Rabi frequency, $2g$, where

$$g = \frac{\mu}{\hbar}\sqrt{\frac{\hbar\omega}{2\epsilon_0 n^2 V}},$$ (S3)

μ is the transition dipole moment, n is the refractive index of the medium, and V is the optical mode volume of the cavity. The cavity energy decay rate is $\kappa = 2\pi \times 30.7\,\text{GHz}$ (Fig. 1D). For simplicity, we assume that the ion is placed at the maximum of the cavity field and optimal polarisation alignment between the cavity mode and the transition dipole.

For the system parameters presented above, the maximal expected coupling is $g_{max} = 2\pi \times 25.5\,\text{MHz}$. The maximum effective Purcell enhancement in the cavity used here is then $\eta_{max} = 143$, which corresponds to a cavity lifetime of $1.87\,\mu\text{s}$. This is in reasonable agreement with the measured lifetime of ion X of $2.27\,\mu\text{s}$, which corresponds to an effective Purcell enhancement of $\beta F_p = 117$. The resulting cavity QED parameters for this system are $(g, \kappa, \gamma_0) = 2\pi \times (22.9\,\text{MHz}, 30.7\,\text{GHz}, 596\,\text{Hz})$. Similar measurements on ion Y give a Purcell-enhanced lifetime of $2.3\,\mu\text{s}$ indicating that ion X and ion Y are nearly identically coupled to the cavity.

In addition to enhancing the emission rate, the Purcell effect leads to preferential emission of photons into the cavity mode from which they can be more readily collected. The fraction of the ion emission into the cavity mode, P_{cav}, is given by the ratio of emission into the cavity to the total emission rate:

$$P_{cav} = \frac{\beta F_p}{1 + \beta F_p}.$$ (S4)

The measured Purcell enhancement corresponds to $P_{cav} = 99.1\%$.

Ultimately, the Purcell-enhanced lifetime of the ion sets the limit on the achievable rate of indistinguishable photon emission. For the case of continuous excitation of the ion, an upper bound for this rate is given as $P_{tot}/2T_1$, where P_{tot}

is the overall detection efficiency and T_1 is the Purcell-enhanced lifetime. For this device, this gives an upper bound of ~ 2.5 kcps. A factor of ten improvement to the detection efficiency should be feasible in this platform as discussed in Section 1, which would enable 25 kcps count rates for the lifetimes achieved here. By increasing the Q/V of the cavity through improved fabrication or alternative device architectures, we expect to further reduce the optical lifetime and increase the achievable photon emission rates.

3.2 Modification of branching ratio in cavity

The Purcell enhancement in this system improves the cyclicity of the optical transitions. In this context, cyclicity describes the probability that an excited ion will return to its original ground state upon emission of a photon. High cyclicity is essential for single-shot readout in which the qubit state is assigned based on the number of photons detected during repeated optical excitation of the ion.

We assume the ion starts in $|1\rangle_g$ and is excited to $|0\rangle_e$ on transition A. Once in the excited state, the ion can decay via the 984.5 nm transition back to $|1\rangle_g$ with rate $\gamma_\parallel$ or to $|aux\rangle_g$ with $\gamma_\perp$. It can also decay back to the ground state through the other crystal field levels with rate γ_{other}. The total excited state decay rate γ_0 is then

$$\gamma_0 = \gamma_\parallel + \gamma_\perp + \gamma_{other}. \tag{S5}$$

For an ion in the bulk crystal, the overall branching ratio for decay via A is $\beta_\parallel = \gamma_\parallel/\gamma_0 \approx 0.35$ (*S10*). The cavity enhances the emission rate for $E \parallel c$ by $1 + F_p$, which results in a cavity-enhanced branching ratio for this transition:

$$\beta_\parallel^{cav} = \frac{(1 + F_p)\beta_\parallel \gamma_0}{\gamma_{cav}} = \frac{(1 + F_p)\beta_\parallel}{1 + F_p\beta_\parallel} \tag{S6}$$

$$= 1 - (1 - \beta_\parallel) \frac{T_1^{cav}}{T_1^{bulk}}. \tag{S7}$$

From the observed cavity lifetime of $T_1^{cav} = 2.3\,\mu$s and bulk lifetime of $T_1^{bulk} = 267\,\mu$s, we predict a branching ratio in the cavity of $\beta_\parallel^{cav} \geq 0.994$. Here we have assumed that decay through the other crystal field levels will bring the ion to a ground state other than $|1\rangle_g$ to provide a lower bound to the expected branching ratio in the cavity.

The optical branching ratio is measured directly by initialising the ion into $|1\rangle_g$ and measuring the optical pumping of the population as a function of the number of optical read pulses applied. Fig. S5 plots the cumulative PL counts, N_c, observed as a function of number of read pulses, N_p, on A for the ion initialised into $|1\rangle_g$. This is fit to the form

$$N_c(N_p) \propto \frac{1 - \beta_{eff}^{N_p}}{1 - \beta_{eff}}, \tag{S8}$$

where β_{eff} is the effective branching ratio $\beta_{eff} = (1 - p_{exc}) + p_{exc}\beta_\parallel^{cav}$ to take into account the excitation probability, p_{exc}, of the readout pulses. This gives $\beta_{eff} = 0.997$, which is in agreement with the predicted bound on the branching ratio from the lifetime. Using $p_{exc} \approx 0.94$ determined from optical Rabi measurements, $\beta_\parallel^{cav} = 0.9968$. Further improvements to the cyclicity could be achieved with larger Purcell enhancement in cavities with higher quality factors.

4 Spectral diffusion and post-selection

Extended Data Fig. 3A shows an optical echo measurement on transition A, which gives a coherence time of $T_{2,o} = 4.1 \pm 0.2\,\mu$s. The considerably shorter optical Ramsey coherence time (Fig. 2E) indicates that the measured $T_{2,o}^*$ is limited by quasi-static fluctuations in the frequency of transition A. The current $T_{2,o}^*$ will be detrimental to photon indistinguishability, but can be improved, for instance, by using post-selection to ensure the ion is on resonance with the excitation pulse (*S18*). We demonstrate the possibility of this approach in this system by post-selecting Ramsey measurements based on number of photons, n_c, detected during a subsequent probe sequence consisting of a series of resonant, low power optical pulses on the transition A.

Extended Data Fig. 3B shows the results of postselected resonant Ramsey measurements, where improvements in $T_{2,o}^*$ are observed for increasing number of probe photons detected. Extended Data Fig. 3C shows similar measurements
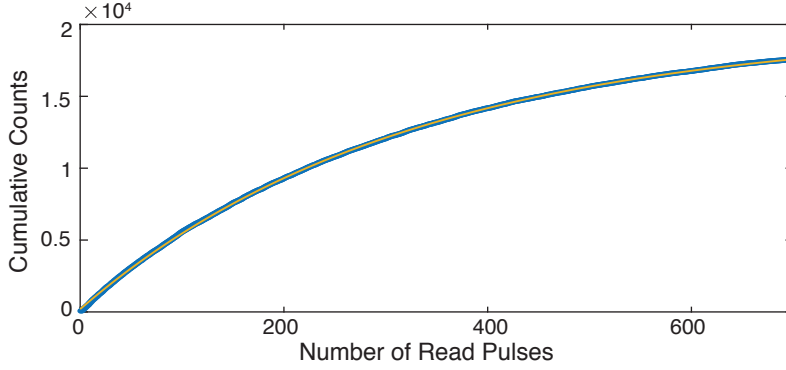
Figure S5: Measurement of optical branching ratio extracted from SSRO measurements. The ion is initialised into state $|1\rangle_g$ and the population in $|1\rangle_g$ is measured with a series of readout pulses. The cumulative sum of total counts measured after each read pulse in the experiment is plotted as function of the number of read pulses (blue). Fit (yellow) gives $\beta_{eff} = 0.997$.

with the excitation pulses detuned by 1 MHz to give rise to characteristic Ramsey fringes, verifying that this indeed corresponds to a coherence decay. Post-selecting with $n_c = 2$ leads to a $T^*_{2,o}$ of 1.0 ± 0.1 μs albeit with approximately 84% of the Ramsey experiments discarded. Higher collection efficiency in future devices will further increase the ability to discriminate when the ion is on resonance and should enable further improvements in $T^*_{2,o}$ using this or similar post-selection techniques.

One possible cause of these quasi-static fluctuations in the optical transition frequency is the magnetic dipole-dipole, or superhyperfine (SHF), interaction between the Yb electron spin and host nuclei, specifically vanadium ($I_V = 7/2$) and yttrium ($I_Y = 1/2$). Coupling to the two nearest vanadium ions is expected to dominate due to the $1/r^3$ scaling of the magnetic dipole-dipole interaction and the relative size of the nuclear g-factors ($g_V = 1.5$ and $g_Y = -0.27$) (S19). Simulations of the optical transition that take into account the superhyperfine interaction give a broadening on A of < 50 kHz (FWHM). This does not fully account for the observed 370 ns $T^*_{2,o}$ time, which corresponds to an 860 kHz linewidth. To verify that $T^*_{2,o}$ is not limited by temperature dependent mechanisms in this range, we repeated the optical Ramsey measurements up to 1 K (Fig. S6) and did not observe degradation of $T^*_{2,o}$. Further investigation of the limits of the $T^*_{2,o}$ due to the SHF mechanism and other factors, such as the second-order DC stark shift of this transition, will be the subject of future research.
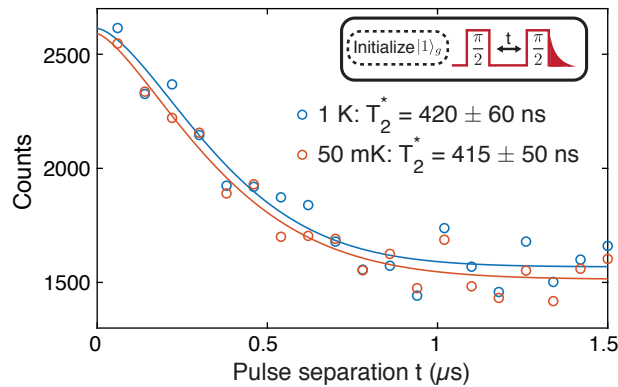

Figure S6: Temperature dependence of optical Ramsey measurement on transition A. Fits (solid line) give $T^*_{2,o} = 415 \pm 50$ ns at 50 mK (red) and $T^*_{2,o} = 420 \pm 60$ ns at 1 K (blue).

5 Additional spin measurements

5.1 Optically-detected magnetic resonance

Optically-detected magnetic resonance (ODMR) measurements were performed on the ground state spin transition $|0\rangle_g \leftrightarrow |1\rangle_g$ for initial calibration of the spin transition frequencies and to bound the coherence time. For this measurement, the ion is initialised into state $|0\rangle_g$, a 160 μs long microwave pulse is applied, and the population in state $|1\rangle_g$ is read out optically. Fig. S7 shows a series of ODMR frequency scans on ion Y performed at successively lower microwave powers to reduce the effects of power broadening. At the lowest microwave power used, we measure a linewidth (full-width-half-maximum) of 48 kHz. This places a lower bound on the spin $T_{2,s}^*$ time of 6.6 μs, which is in agreement with the spin $T_{2,s}^*$ measured directly using a Ramsey sequence. From this and similar measurements on ion X, we extract the qubit transition frequencies of ion X and Y to be 674.48 MHz and 673.24 MHz respectively (the inhomogeneous linewidth of this transition measured in bulk 100 ppm ^{171}Yb:YVO is <1 MHz).

The asymmetric profile of the ODMR spectrum is attributed to second-order perturbations of the qubit transition by magnetic dipole-dipole (superhyperfine) interactions with nearby nuclear spins (yttrium and vanadium). To verify this asymmetry is due to the superhyperfine interaction, the energy level structure of the $|0\rangle_g \leftrightarrow |1\rangle_g$ transition was modelled by introducing magnetic dipole-dipole coupling of the Yb electron spin to neighbouring nuclear spins (*S19*). Fig. S7 plots the simulated spectrum due to coupling with 3 nearest vanadium and 1 nearest yttrium, which shows good agreement with the experimental results. Further simulations of the complete spin structure with additional nuclei were not performed due to limited computational resources, but we note that this observed spectrum is dominated by coupling to the neighbouring vanadium.
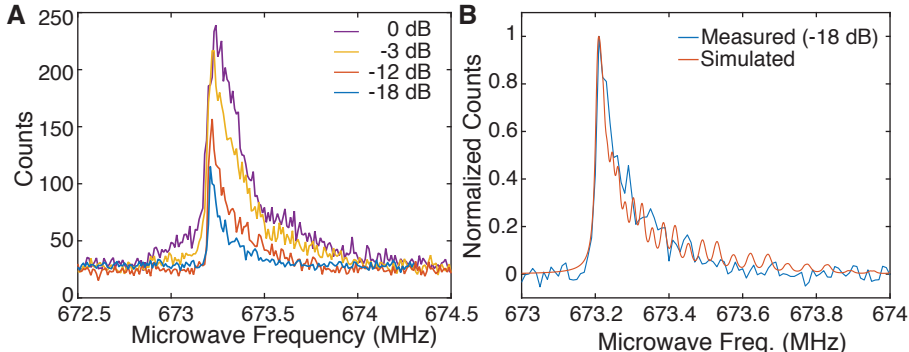

Figure S7: A) Optically-detected magnetic resonance on the $|0\rangle_g \rightarrow |1\rangle_g$ transition. The ion is optically pumped into $|0\rangle_g$, a microwave pulse is applied, and the population in $|1\rangle_g$ is optically read out as a function of microwave frequency. The ODMR signal is measured with increasing attenuation of the microwave pulse to minimise the effects of power broadening. B) Simulated ODMR spectrum (red) that takes into account superhyperfine interaction with 4 neighbours (3V, 1Y) to verify the form of the experimentally observed ODMR signal (blue) is expected. Here, each individual simulated transition is plotted with 15 kHz of broadening.

5.2 Magnetic field dependence of spin coherence

As described in the main text, at zero field the hyperfine interaction gives rise to mixed electron-nuclear spin states of the form $|1\rangle = \frac{1}{\sqrt{2}}(|\uparrow\Downarrow\rangle + |\downarrow\Uparrow\rangle)$ and $|0\rangle = \frac{1}{\sqrt{2}}(|\uparrow\Downarrow\rangle - |\downarrow\Uparrow\rangle)$. These states have zero net magnetic moment and are thus first-order insensitive to perturbations by the Zeeman interaction. Transitions that are first-order insensitive to magnetic fields are often referred to in the rare-earth literature as ZEFOZ transitions (as they have zero first-order Zeeman shift) (*S20*). This reduces the sensitivity of transitions involving these states to magnetic field fluctuations that arise from host nuclei and other rare-earth ions in the crystal (*S11, S21*). In this case, the magnetic field sensitivity of these transitions, and thus, coherence time is determined by the second-order Zeeman interaction (*S20*).

The spin Hamiltonian predicts an increased magnetic field sensitivity for these transitions as an external DC magnetic field is applied, and thus, a reduction in coherence time (*S11*). This is investigated in Fig. S8, which shows the measured qubit coherence time for a magnetic field applied along the *a*-axis. A decrease in coherence time is

observed away from zero field, which provides confirmation that magnetic field sensitivity plays a dominant role in the coherence time. While not explored here, the high magnetic field regime offers the possibility of longer optical and spin coherence times due to reduced magnetic field sensitivity at the expense of weaker spin transition strengths (*S10*).
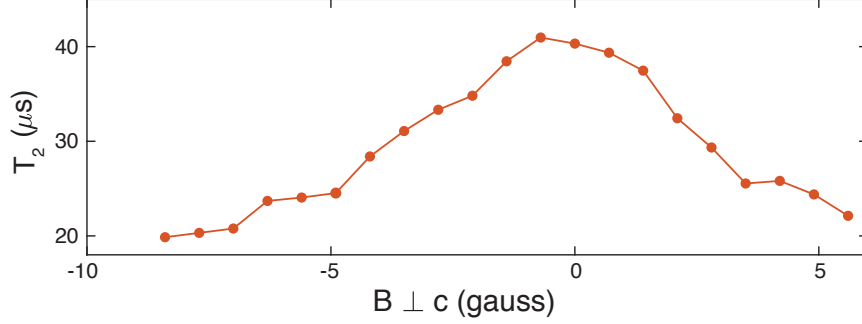

Figure S8: Coherence of $|0\rangle_g \leftrightarrow |1\rangle_g$ measured using a spin-echo sequence for varying magnetic fields applied perpendicular to the *c*-axis of the crystal.

5.3 Noise spectroscopy and dynamical decoupling

This section describes addition measurements performed to understand and prolong the spin coherence. The red trace in Extended Data Fig. 4B shows a Hahn echo measurement on the $|0\rangle_g - |1\rangle_g$ transition with a coherence time of $T_{2,s} = 44 \pm 2\,\mu$s. The stretched-exponential decay is indicative of slow fluctuations in the ion's magnetic environment (*S22*), which are attributed to a nuclear spin bath consisting of lattice spins (specifically $I_V = 7/2$ and $I_Y = 1/2$). The coherence time in this case can be extended by applying dynamical decoupling (DD) pulse sequences such as the Carr-Purcell-Meiboom-Gill (CPMG) pulse sequence, which takes the form (*S23*)

$$\left(\frac{\pi}{2}\right)_y - (\tau - \pi_x - \tau)^N - \left(\frac{\pi}{2}\right)_{-y}. \tag{S9}$$

This sequence can be thought of as a multi-pulse analog to the spin echo technique that extends coherence times by high-pass filtering environmental noise on a frequency scale $\omega \sim 1/\tau$. This sequence can also be treated as a frequency-domain noise filter of the form derived in (*S24*).

The blue trace in Extended Data Fig. 4B shows a measurement of spin coherence using a CPMG pulse sequence with eight π pulses, plotted as a function of the π pulse separation time 2τ. Periodic collapses and revivals in CPMG coherence are observed, which is indicative of a narrow-band noise source at 340 kHz. This is currently attributed to coupling to nearby nuclear spins (similar signatures have been observed with nitrogen vacancy centers weakly coupled to ^{13}C nuclear spins (*S25, S26, S27*)), but further investigations will be the subject of future work. By operating with pulse separations at integer multiples of the coherence revival time, the spin-qubit is effectively decoupled from this narrowband noise as shown in Fig. 3C.

To further study the coherence time limitations of this transition, we follow the procedure outlined in (*S28*). In Extended Data Fig. 4A , the CPMG coherence time is plotted as a function of the number of π pulses in the CPMG sequence (*N*). We extract a power-law dependence of the form $T_{2,s} \propto N^{0.70\pm0.01}$. This indicates a noise spectral density of the form $S(\omega) \propto \omega^{-2.3\pm0.1}$, which agrees well with the expected $S(\omega) \propto \omega^{-2}$ for coupling to a dipolar spin bath approximated by a classical source of Ornstein-Uhlenbeck noise (*S29*).

The combined requirements of decoupling from narrowband noise and minimising the pulse separation time to filter out $1/\omega^2$ noise identifies an optimal pulse separation of $2\tau = 5.74\,\mu$s. By measuring the decay in coherence as a function of CPMG pulse number at this optimal pulse separation, we obtain a $T_{2,s}$ time of 31 ± 3 ms (Fig. 3D).

The CPMG sequence performs single-axis decoupling; it is only robust to pulse errors for initial states parallel to the x-axis of the Bloch sphere. CPMG sequences are thus unsuitable for preservation of arbitrary quantum states. For instance, repeating this sequence with an initial $(\pi/2)_x$ pulse (i.e. y-directed initial state) leads to a reduction in coherence time by two orders of magnitude due to rapid accumulation of pulse errors ($T_{2,s} = 240\,\mu$s). We can mitigate

this effect by using sequences with decoupling pulses applied along multiple axes (*S30*). As an example of this, Fig. S9 shows measurements of coherence times up to 4 ms using the XY-8 pulse sequence:

$$\left(\frac{\pi}{2}\right) - [\tau\text{-}\pi_x\text{-}2\tau\text{-}\pi_y\text{-}2\tau\text{-}\pi_x\text{-}2\tau\text{-}\pi_y\text{-}2\tau\text{-}\pi_y\text{-}2\tau\text{-}\pi_x\text{-}2\tau\text{-}\pi_y\text{-}2\tau\text{-}\pi_x\text{-}\tau]^N - \left(\frac{\pi}{2}\right).$$ (S10)

This sequence has been demonstrated to preserve coherence for arbitrary initial states (*S31*), which is a crucial requirement for using this transition as a quantum memory.
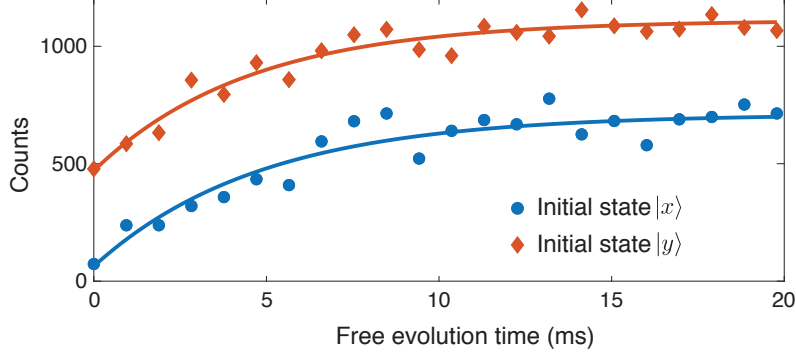

Figure S9: Decay of coherence using XY-8 sequence for two phases of the initial superposition state. Scans are offset by 500 counts for clarity.

5.4 Discussion of spin lifetime

Spin lifetime measurements were performed at cryostat temperatures up to 1.2 K. We observed less than a factor of two change in the decay rate on the $|0\rangle_g \leftrightarrow |1\rangle_g$ transition over this range, indicating that this is unlikely to be dominated by a phonon-assisted process that would be expected to scale strongly with temperature (*S32*). Instead, we postulate a direct spin-spin relaxation mechanism mediated by magnetic dipole-dipole interactions with other $^{171}\text{Yb}^{3+}$ ions in the crystal. This is expected to be a significant effect in this system due to the narrow inhomogeneous linewidths of the spin transition at zero field (<1 MHz). Furthermore, the large difference between the $|0\rangle_g \leftrightarrow |1\rangle_g$ and $|0\rangle_g, |1\rangle_g \leftrightarrow |aux\rangle_g$ relaxation rates (Extended Data Fig. 5) is in agreement with the g^4 scaling for this mechanism (*S33*) (corresponding g-factors for these two transitions are -6.08 and 0.85, respectively (*S34*)).

More measurements are necessary to further investigate the underlying relaxation mechanism. For lifetimes dominated by direct spin flip-flops, we expect that reducing the population of resonant ^{171}Yb ions in the $|0\rangle_g, |1\rangle_g$ manifold will increase the $|0\rangle_g \leftrightarrow |1\rangle_g$ lifetime thereby also improving the CPMG coherence time that is currently approaching the lifetime limit. This could be accomplished by optically initialising other ^{171}Yb ions in the device into the $|aux\rangle_g$ state, or investigating samples with lower doping concentrations and increased spin inhomogeneity (*S35*).

6 Single-shot readout fidelities

6.1 Photon count distributions and readout fidelity

For single-shot readout, the state of the ion is assigned based on the number of photons detected during an optical readout period consisting of a series of optical excitation pulses on transition A. We choose a photon number cutoff, n_c, and assign the state of the ion to $|1\rangle$ if we measure $\geq n_c$ photons during the readout period and to $|0\rangle$ is we measure $< n_c$ photons. As mentioned earlier, the qubit is optically read out on transition A, because transition E overlaps with the optical transition of the zero-spin isotope.

The fidelity F_i of this readout is the probability of obtaining the measurement outcome i after initialising into i: $F_i = 1 - \epsilon_i$, where ϵ is the error of assignment given by:

$$\epsilon_0 = \sum_{k=n_c}^{\infty} P_{|0\rangle}(k)$$ (S11)

and

$$\epsilon_1 = \sum_{k=0}^{n_c-1} P_{|1\rangle}(k). \tag{S12}$$

Here, $P_{|i\rangle}(k)$ is the photon count distribution describing the probability of measuring k counts with the ion in $|i\rangle$.

The photon count distribution for the ion initialised in $|0\rangle_g$ will be determined by the background count rate Γ_{bg} due to detector dark counts, light leakage, or fluorescence from other ions in the crystal. We assume these background counts follow a Poisson distribution with the average photon number $\bar{N}_{bg} = \Gamma_{bg} N_r t_r$ detected in N_r readout pulses with integration time t_r per pulse.

The photon count distribution for the ion in $|1\rangle_g$ will be a convolution of the counts due the ion and the background:

$$P_{|1\rangle_g}(N_{tot} = n) = \sum_{k=0}^{n} P(N_{ion} = k)P(N_{bg} = n - k), \tag{S13}$$

where $N_{tot} = N_{bg} + N_{ion}$ is the total number of counts measured due to counts from the ion, N_{ion}, and the background N_{bg}. The photon count distribution from the ion will be determined by the cyclicity of transition A and overall detection efficiency. Upon excitation, the ion has a probability of optically decaying to $|aux\rangle$ given by $p_f = 1 - \beta_{eff}$, where β_{eff} is the effective branching ratio for decay on the $|0\rangle_e \to |1\rangle_g$ transition discussed in Section 3.2. The total number of successful read pulses N_r during a given readout sequence before the ion is optically pumped follows a geometric distribution:

$$P(N_r = k) = (1 - p_f)^k p_f, \tag{S14}$$

where $k = \{0, 1, 2, 3, ...\}$. As a result, the total number of counts due to the ion, N_{ion}, will be a randomly stopped sum of N_r pulses that are sampled binomially with total system detection efficiency p_{tot}:

$$P(N_{ion} = k) = \sum_{N_r=k}^{\infty} P(N_{ion} = k|N_r)P(N_r) \tag{S15}$$

$$= \sum_{N_r=k}^{\infty} \binom{N_r}{k} p_{tot}^k (1 - p_{tot})^{(N_r-k)} (1 - p_f)^{N_r} p_f. \tag{S16}$$

This can be written as another geometric distribution

$$P(N_{ion} = k) = (1 - p_n)^k p_n, \tag{S17}$$

where $p_n = \frac{p_f}{p_{tot}+p_f-p_{tot}p_f}$. The form above assumes that readout is done using a sufficient number of read pulses such that the ion is optically pumped away by the end of the sequence with high probability and we can thus approximate the distribution as geometric.

To measure the photon count distribution and assign a readout fidelity, the ion is initialised into $|0\rangle_g$ or $|1\rangle_g$ and the readout procedure is repeated many times to acquire adequate statistics. Fig. 4b shows one such photon count histogram where 400 read pulses were used per sequence, which is in good agreement with the expected form for the distributions given above. Using a cutoff of $n_c = 1$, we extract $F_0 = 96.1\%$ and $F_1 = 64.0\%$ for an average fidelity of $F_{avg} = (F_0 + F_1)/2 = 80.0\%$. This fidelity is not strictly the readout fidelity, but the combined initialisation and readout fidelity. The low dark and leakage counts in this system enables high-fidelity readout when the ion is initialised into $|0\rangle_g$, but the geometric distribution of ion counts due to the finite branching ratio and detection efficiency limits F_1. Furthermore, detection of zero photons during the readout period does not distinguish between the ion being in $|aux\rangle$ or $|0\rangle$.

6.2 Conditional readout fidelities

We implement a conditional readout procedure described in the text to overcome the difference in readout fidelity between the qubit states and improve the overall readout fidelity. We read out the state of the ion using a series of optical π pulses, apply a π pulse to the $|0\rangle_g \to |1\rangle_g$ transition, and read out the state of the ion again. The state of the ion is determined during each readout period as described above and labeled as $|ab\rangle$, where $a(b)$ is the outcome of the

first (second) readout. The initial state is conditionally assigned to $|0\rangle_g$ on the observation of $|01\rangle$ and to $|1\rangle_g$ on the observation of $|10\rangle$. This procedure takes advantage of the high F_0 fidelity, which corresponds to a high probability of the ion being in $|1\rangle_g$ if one or more photons are detected. Conditionally assigning the state on at least one count in the first or second readout period also ensures that the ion was in the qubit subspace prior to the measurement.

The expected fidelity of the conditional readout can be determined by the fidelities F_i of the first and second readout sequence (Table S1). These forms assume that the readout fidelity is identical for the first and second readout sequences, but in general the overall fidelity of the first readout will be higher due to spin relaxation and microwave pulse errors. The conditional readout fidelity is

$$F_{cond} = \frac{F_0 F_1}{F_0 F_1 + (1 - F_1)(1 - F_0)}. \tag{S18}$$

The improved fidelity comes at a reduced success rate of assigning the ion to either qubit state. The probability of measuring $|10\rangle$ or $|01\rangle$ using the conditional readout procedure is

$$P_{success} = F_0 F_1 + (1 - F_1)(1 - F_0). \tag{S19}$$

Fig. S10 shows the fidelity of the single and conditional readout along with the success rate for increasing numbers of readout pulses. For the data presented in Figs. 4B and 4C of the main text, 400 read pulses are used in each sequence, which corresponds to the plateau in the success rate with $F_{1,avg} = 80\%$, $F_{cond} = 95.3\%$, and $P_{success} = 62.6\%$. Slightly higher fidelities are achieved with fewer pulses at a reduced success rate. Further improvements to the readout fidelity will be enabled by higher overall detection efficiencies and by further enhancements of the branching ratio, which should be achievable in a higher Q cavity.

Table S1: Probability of outcome $|ab\rangle$ of the conditional single-shot readout protocol for ion prepared in $|i\rangle$ in terms of readout fidelities for a single series of pulses. These forms assume identical readout fidelities for the first and second readout sequences.

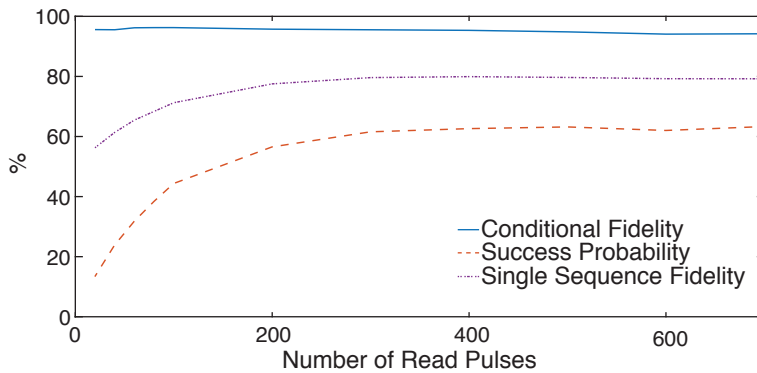| Measured	Prepared	
$|ab\rangle$	$|0\rangle$	$|1\rangle$
$|00\rangle$	$F_0(1 - F_1)$	$(1 - F_1)F_0$
$|01\rangle$	$F_0 F_1$	$(1 - F_1)(1 - F_0)$
$|10\rangle$	$(1 - F_0)(1 - F_1)$	$F_1 F_0$
$|11\rangle$	$(1 - F_0)F_1$	$F_1(1 - F_0)$

Figure S10: Dependence of single-shot readout fidelity as a function of number of read pulses for the single readout sequence (purple, dot-dashed) and the conditional sequence (blue, solid). The success probability of observing the ion within the qubit subspace (i.e. measuring $|10\rangle$ or $|01\rangle$) using the conditional readout procedure is shown in red (dashed).

References

[S1] F. Marsili, *et al.*, *Nature Photonics* **7**, 210 (2013).

[S2] T. Zhong, *et al.*, *Science* **357**, 1392 (2017).

[S3] C. T. Nguyen, *et al.*, *Physical Review Letters* **123**, 183602 (2019).

[S4] E. Miyazono, I. Craiciu, A. Arbabi, T. Zhong, A. Faraon, *Optics Express* **25**, 2863 (2017).

[S5] A. M. Dibos, M. Raha, C. M. Phenicie, J. D. Thompson, *Physical Review Letters* **120**, 243601 (2018).

[S6] S. Gröblacher, J. T. Hill, A. H. Safavi-Naeini, J. Chan, O. Painter, *Applied Physics Letters* **181104** (2013).

[S7] T. G. Tiecke, *et al.*, *Optica* **2**, 70 (2015).

[S8] S. Mosor, *et al.*, *Applied Physics Letter* **87**, 10 (2005).

[S9] A. Abragam, B. Bleaney, *Electron Paramagnetic Resonance of Transition Ions* (Oxford University Press, Oxford, 2012).

[S10] J. M. Kindem, *et al.*, *Physical Review B* **80**, 1 (2018).

[S11] A. Ortu, *et al.*, *Nature Materials* **17**, 671 (2018).

[S12] R. M. Macfarlane, *Journal of Luminescence* **125**, 156 (2007).

[S13] S. C. Kitson, P. Jonsson, J. G. Rarity, P. R. Tapster, *Phys. Rev. A* **58**, 620 (1998).

[S14] G. Sallen, *et al.*, *Nature Photonics* **4**, 696 (2010).

[S15] F. J. P. Schuurmans, P. D. Vries, A. Lagendijk, *Physics Letters A* pp. 472–477 (2000).

[S16] J. M. Kindem, Quantum Nanophotonics with Ytterbium in Yttrium Orthovanadate, Ph.D. Thesis, California Institute of Technology (2019).

[S17] B. Henderson, G. Imbush, *Optical spectroscopy of inorganic solids* (Oxford University Press, 2006).

[S18] L. Robledo, H. Bernien, I. V. Weperen, R. Hanson, *Physical Review Letters* **177403**, 1 (2010).

[S19] B. Car, L. Veissier, A. Louchet-Chauvet, J. L. Le Gouët, T. Chanelière, *Physical Review Letters* **120**, 1 (2018).

[S20] D. L. McAuslan, J. G. Bartholomew, M. J. Sellars, J. J. Longdell, *Physical Review A* **85**, 032339 (2012).

[S21] J. V. Rakonjac, Y.-H. Chen, S. P. Horvath, J. J. Longdell, *arXiv:1802.03862* (2018).

[S22] J. R. Klauder, P. Anderson, *Physical Review* **125** (1961).

[S23] S. Meiboom, D. Gill, *Review of Scientific Instruments* **29**, 688 (1958).

[S24] Ł. Cywiński, R. M. Lutchyn, C. P. Nave, S. Das Sarma, *Physical Review B* **77**, 1 (2008).

[S25] N. Zhao, *et al.*, *Nature Nanotechnology* **7**, 657 (2012).

[S26] T. H. Taminiau, *et al.*, *Physical Review Letters* **109**, 137602 (2012).

[S27] S. Kolkowitz, Q. P. Unterreithmeier, S. D. Bennett, M. D. Lukin, *Physical Review Letters* **109**, 1 (2012).

[S28] J. Medford, *et al.*, *Physical Review Letters* **108**, 086802 (2012).

[S29] V. V. Dobrovitski, A. E. Feiguin, R. Hanson, D. D. Awschalom, *Physical Review Letters* **102**, 1 (2009).

[S30] T. Gullion, D. B. Baker, M. S. Conradi, *Journal of Magnetic Resonance (1969)* **89**, 479 (1990).

[S31] G. De Lange, Z. Wang, S. Riste, V. V. Dobrovitski, R. Hanson, *Science* **330**, 60 (2010).

[S32] E. Z. Cruzeiro, *et al.*, *Physical Review B* **95**, 205119 (2017).

[S33] T. Böttger, C. W. Thiel, Y. Sun, R. L. Cone, *Physical Review B* **73**, 075101 (2006).

[S34] U. Ranon, *Physics Letters A* **28**, 228 (1968).

[S35] S. Welinski, *et al.*, *Optical Materials* **63**, 69 (2017).